Materials Advances

Accepted Manuscript

This article can be cited before page numbers have been issued, to do this please use: M. R. Puthalath, S. Zaman, K. Pawar and S. Shahgaldi, *Mater. Adv.*, 2026, DOI: 10.1039/D6MA00453A.

ROYAL SOCIETY OF CHEMISTRY

rsc.li/materials-advances

View Article Online
DOI: 10.1039/D6MA00453A

Stabilizing Low-Iridium Anode Catalysts via Boron Carbon Nitride Supports for Efficient PEM Water Electrolysis

*Muhammad Rahees Puthalath†, Shahid Zaman†, Kaushiki Pawar, and Samaneh Shahgaldi**

Hydrogen Research Institute, University of Québec Trois Rivieres (UQTR), Trois Rivieres, Quebec G8Z 4M3, Canada.

† These authors contributed equally to this work

Corresponding author: Samaneh Shahgaldi (Samaneh.shahgaldi@uqtr.ca)

Abstract: The high cost and limited durability of iridium (Ir)-based anode catalysts are huge barriers for the large-scale applications of proton exchange membrane water electrolyzers (PEMWEs). Employing a conductive and corrosion resistant catalyst supports can mitigate these issues by maximizing the Ir utilization and long-term stability. This work reports boron carbon nitride (BCN) catalyst support for Ir nanoparticles that exhibits improved oxygen evolution reaction kinetics and excellent stability in PEMWEs. Ir-BCN prepared via facile solid-state synthesis of BCN followed by Ir nanoparticles deposition via polyol synthesis shows a high oxygen evolution activity achieving an overpotential of 240 mV at 10 mA cm^2. More importantly, the Ir-BCN as anode catalyst layer in PEMWEs shows high performance and improved stability compared to IrO_x-TKK based catalyst. The detailed voltage breakdown analysis revealed that the low kinetic and mass transport losses of Ir-BCN based catalyst layer contribute to the improved cell performance. Similarly, the corrosion test results also reveal a significantly low corrosion current for Ir-BCN than IrO_x-TKK, highlighting its enhanced durability. This work highlights the combination of high conductivity, corrosion resistance, and scalable synthesis of BCN as a catalyst support for durable anode catalysts in PEMWEs.

Keywords: *PEM water electrolyzer; Low-Iridium; Catalyst support, Corrosion resistant, Boron carbon nitride, Voltage breakdown, Polarization curve.*

View Article Online
DOI: 10.1039/D6MA00453A

1. Introduction:

With growing urgency to reduce dependence on fossil fuels, transitioning to sustainable green hydrogen has become a vital pathway for decarbonizing transportation and other high-emission industries.[1-3] Among the different hydrogen production methods, water electrolysis via renewable energy is the most sustainable method that produce high purity green hydrogen.[4-6] Alkaline water electrolyzers, proton exchange membrane water electrolyzers (PEMWEs), solid oxide electrolyzers, and anion exchange membrane electrolyzers are the major electrolyzer technologies for green hydrogen production.[7] While all these technologies have their own advantages, the PEMWEs are considered promising due to their wide operational current density, low operating temperature, low ohmic losses, high efficiency and high purity hydrogen.[8,9] Membrane electrode assembly (MEA) is the core part of PEMWEs, which consist of anode and cathode catalyst layers on proton exchange membrane sandwiched between porous transport layer (PTL) and gas diffusion layer (GDL).

The anodic catalyst layer is the most crucial component due to sluggish oxygen evolution reaction (OER) kinetics catalysed by the costly iridium based catalysts.[10,11] Due to the scarce resources and high cost of Ir based catalyst, the large scale hydrogen production with high Ir loadings (~1-2 mg cm^{-2}) is unaffordable compared to traditional energy sources.[12,13] Therefore, reducing the Ir loadings is indispensable for large scale applications of PEMWEs. Meanwhile, despite the high performance of various low Ir-loading of Ir based catalysts, their limited stability under harsh PEMWEs conditions is still a huge barrier to meet the long-term applications.[14-16] Thus, it is of significant importance to reduce Ir loadings without compromising catalyst stability.[17,18]

Employing a conductive and corrosion-resistant support helps to overcome these challenges. Catalyst supports improve Ir utilization and preserve the structural integrity of catalyst layers with low Ir loadings, which is difficult to achieve with unsupported catalysts that tend to dissolve rapidly at low Ir loadings. A good support provides better dispersion that increases the active sites density, improves charge transfer properties of catalyst and enhances the structural stability of the catalyst through a strong metal support interaction.[19-21] Thus, loading Ir nanoparticles (NPs) on a conductive, high surface area and corrosion resistant catalyst support can enhance the stability of anode catalysts in PEMWEs.[22,23] Carbon is widely used as catalyst support in electrocatalysis due to its high surface area, facile surface functionalization and excellent conductivity.[24,25] However, due to higher operating voltage in PEMWE, carbon is prone to corrosion and oxidation.[16] Thus, replacing the carbon with other corrosion resistant materials or modifying its chemical structure could improve its durability

View Article Online
DOI: 10.1039/D6MA00453A

as a catalyst support.[26] Graphitic carbon nitride (GCN) has been reported as a good corrosion resistant support material under acidic OER conditions.[27-30] For instance, a homogeneous confinement of IrO_2 NPs on GCN sheets shows enhanced OER performance, where nitrogen rich environment of GCN induce a strong electronic interaction with IrO_2 and improve the catalyst activity.[27] Nitrogen defects on GCN surface enhance the electrical conductivity and alters the surface properties that provide strong anchoring sites for IrO_2 NPs. Similarly, doping heteroatoms in GCN could further improve the electronic structure and alters the physicochemical properties of GCN.[31] For instance, doping boron into GCN could further enhance the thermal stability and oxidation resistance.[32,33] B atom activates the N sites due to higher electronegativity of B-N bond compared to C-N, resulting in more strengthening of Ir-N coordination on the BCN surface.[34] Thus, incorporating B into carbon nitrides could enhance the intrinsic activity and stability via strong metal support interaction and could be used as a potential catalyst support for OER catalysts in PEMWEs. Although carbon nitrides are known for their excellent stability and conductivity, they have rarely been explored as catalyst supports for anode catalyst layers in PEMWEs. In a recent work, BCN has been used as a catalyst support for Ir catalyst in PEMWE.[35] The synthesized Ir-BCN catalyst exhibits excellent half-cell performance and stability. While the same catalyst shows good PEMWE performance yet, the test conditions such as acidic electrolyte (0.1 M $HClO_4$) and durability of merely 50 hours at 0.2 A cm^{-2}, don't reflect the standard operating conditions of PEMWEs. Therefore, current work aims to develop an efficient and durable supported catalyst to improve the anode catalyst performance and stability under standard operating conditions of PEMWEs.[36,37]

In this work, BCN catalyst support is utilized to deposit Ir NPs as anode catalyst layer in PEMWEs. The synthesized BCN supported Ir NPs shows significantly improved stability under standard PEMWEs operating conditions. Thus, bridging the gap between half catalyst assessment and standard PEMWEs operating condition, this study demonstrates the improved anode catalyst performance and stability surpassing the IrOx-TKK based commercial catalyst under standard PEMWE operating conditions. The detailed structural characterizations and pol curves analysis of cell voltage losses along with corrosion testing further validates the excellent performance and stability of the Ir/BCN catalyst in PEMWEs.

2. Experimental and methods

2.1 Preparation of BCN: For preparing BCN, 3.0 g of melamine added with 1.47 g of H_3BO_3 (3:3) and dispersed in deionized water to form a uniform white mixture.[38] The mixture was

View Article Online
DOI: 10.1039/D6MA00453A

dried at 60 °C and grind into powder with an agate mortar. The powdered mixture was annealed at 550 °C in inert atmosphere for 4 hours (with a heat rate 5 °C min^{-1}). The obtained products were washed with deionized water and dried at 60 °C. Finally, the pale-yellow BCN powder was collected and used as catalyst support for Ir nanoparticles deposition in next step.

2.2 Preparation of Ir-BCN: Iridium deposition is carried out by polyol method.[39] The required amount of $IrCl_2$ is added to 30 mL of ethylene glycol followed by few drops of 0.1 M NaOH solution. The mixture was refluxed for 2 hours at a reaction temperature of 170 °C (Inert atmosphere). Another pre-sonicated mixture of BCN in ethylene glycol is added to above solution and refluxed the reaction overnight at 80 °C. Finally, the solution was cooled down naturally and filtered by using vacuum filtration. The obtained product Ir-BCN is washed with deionized water and dried at 60 °C.

2.3 Physical characterization: The surface morphology of the synthesized samples was examined using a Hitachi SU1510 VP scanning electron microscope (SEM), equipped with energy dispersive X-ray spectroscopy (EDS) and operated at an accelerating voltage of 20 kV. EDS was used to analyze surface composition and perform elemental mapping. Detailed morphological analysis was carried out using a Thermo Scientific Talos 200X transmission electron microscope (TEM), which is equipped with an X-FEG source and supports adjustable accelerating voltages ranging from 80 to 200 kV. The X-ray diffraction (XRD) patterns were obtained for BCN and Ir-BCN utilizing the New D8 ADVANCE instrument manufactured by Bruker AXS. This analysis employed both Bragg–Brentano geometry with a full scan between $2\theta = 15°$- 80°, employing Cu kα radiation with a wavelength of 1.54 Å at 40 kV and 30 mA. X-ray photoelectron spectroscopy (XPS) measurements were performed using a PHI Quantes spectrometer with an aluminum anode, providing a photon energy of 1486.6 eV (Kα). Depth profiling was conducted through sequential ion etching. XPS was employed to identify and characterize the material surfaces, providing information on their chemical composition and oxidation states in selected regions.

2.4 Electrochemical half-cell measurements: Catalyst ink was prepared by sonication of 5 mg of the material in 7.5 mL of ethanol, 2.4 mL of IPA, and 10 µL of 5 % Nafion solution. Half-cell OER testing was performed using a catalyst-coated gold electrode (working electrode), graphite (counter electrode), and Reversible Hydrogen Electrode (RHE, reference electrode) in a BioLogic SP-300e Potentiostat. 0.5 M H_2SO_4 used as a catalyst solution. The

View Article Online
DOI: 10.1039/D6MA00453A

results were compared with those of commercially purchased IrO_x-TKK. All the potentials are measured *vs.* RHE.

2.5 Preparation of CCM and single-cell PEM water electrolyzer testing: MEA were prepared using Nafion 115 membrane as the electrolyte, commercial 20 wt% Pt/C catalyst for the cathode, and a synthesized Ir-BCN sample for the anode. The catalysts were converted into inks by mixing the appropriate amount of catalyst material (20 wt% Pt/C and the synthesized sample) with isopropyl alcohol, ultrapure water, and Nafion solution. The mixture was subjected to sonochemical dispersion to ensure uniformity, followed by ball milling for seven days. The resulting homogeneous inks were spray coated onto each side of the Nafion 115 membrane, achieving a Pt 0.5 mg cm^{-2} and Ir mass loading of 0.7 mg cm^{-2}. The MEA was then assembled into a single-cell PEM water electrolyzer with an effective area of 5 cm^2. A commercial IrO_x-TKK based catalyst was also prepared and tested as a reference under identical conditions.

The electrochemical performance of the MEAs was characterized by polarization curves recorded with current densities varying from 0.01 to 3 A cm^{-2} to assess OER activity. Electrochemical impedance spectroscopy (EIS) measurements were conducted, and Nyquist plots were obtained over a frequency range of 100 kHz to 100 mHz with a 10 mV amplitude. Durability testing was performed under a constant current density of 1 A cm^{-2} for 575 hours. All electrochemical evaluations were carried out at a water temperature of 80 °C and a flow rate of 140 Ml min^{-1}, using a Greenlight electrolyser test station.

3. Results and discussion

3.1 Catalyst design and Characterization: BCN support was synthesized by a facile one step annealing followed by the deposition of Ir NPs via polyol synthesis (**Fig. 1a**). The precursors were mixed in deionized water and dried at 60 °C followed by the annealing at 550 °C in inert atmosphere.[38] For Ir deposition, required amount of Ir salt was dissolved in ethylene glycol and refluxed 170 °C (Inert atmosphere), followed by the addition of sonicated mixture of BCN and the reaction was refluxed overnight at 80 °C.[39] The polyol method is less toxic than hydrazine or sodium borohydrate based reduction methods and allows size-controlled nanoparticle synthesis simply by adjusting the reaction pH and temperature, without requiring surfactants.[40] Moreover, the BCN synthesis is facile and scalable for gram scale synthesis and could also be extended to other support materials. The morphology of the Ir supported BCN is analysed by

View Article Online
DOI: 10.1039/D5MA00453A

scanning electron microscopy (SEM) and high-resolution transmission electron microscopy (HRTEM) and energy dispersive spectroscopy (EDS) mapping. The SEM image shows porous lamellar structure of BCN having particle sizes ranging in few hundred micrometres (**Fig. 1b**). Spherical shape Ir NPs are uniformly dispersed over BCN surface are evidenced by TEM image (**Fig. 1c**). The HRTEM image shows the individual Ir NP of 2 nm size within the BCN layers, with the lattice fringes 0.22 nm corresponding to (111) plane of the Ir that matches the planes of face-centered cubic (FCC) Ir (**Fig. 1d**). There are no gaps or interfacial voids visible, due to this coherent interface, the Ir NPs are firmly attached to the BCN support, most likely by chemical or electrical interactions made possible by the BCN's nitrogen-rich domains. Particle size distribution analysis shows that most particles have sizes between 2 and 4 nm, indicating a narrow and uniform particle size distribution (**Fig. 1e**). Furthermore, the composition of the Ir-BCN is studied by EDS mapping where C, B and N are found as base material and the Ir NPs are dispersed on the surface (**Fig. 1f**).

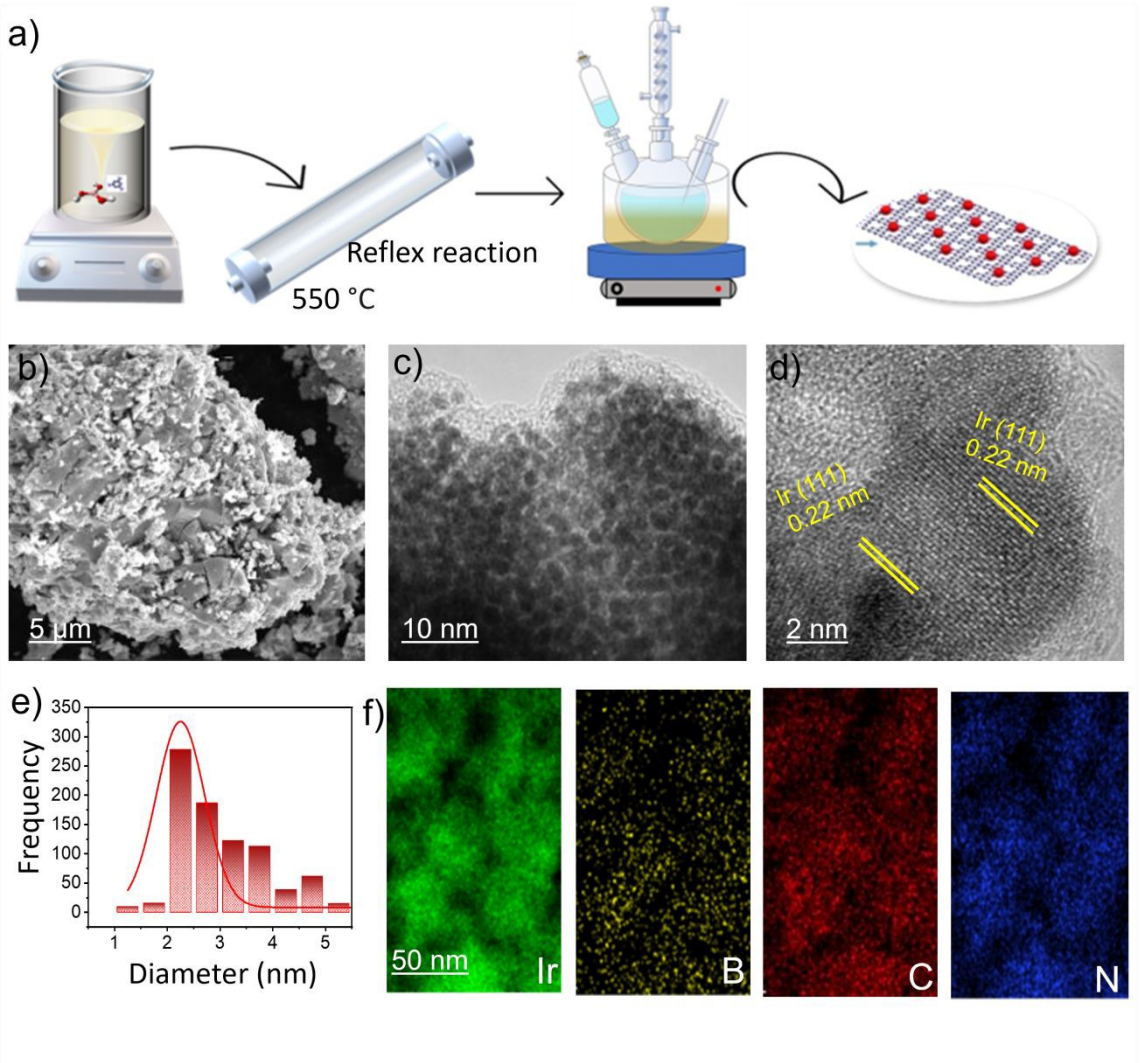

View Article Online
DOI: 10.1039/D0MA00453A

Figure 1. Synthesis and morphology analysis: **a)** Schematic diagram for the synthesis of Ir-BCN, **b)** FESEM images of Ir-BCN **c, d)** TEM and HRTEM images, **e)** Particle size distribution, **f)** EDS elemental mapping of Ir-BCN.

The X-ray Diffraction (XRD) shows the diffraction pattern of BCN and Ir-BCN, where Ir a broadened peak at ~ 41º corresponds to Ir (111) crystal plane demonstrating the Ir incorporation into BCN (**Fig.2 a**). This broadened diffraction peak can be assigned to the Ir (111) reflection of face-centered cubic metallic Ir, in agreement with the standard Ir diffraction pattern (JCPDS card No. 06-0598).[41,42] A broadened Ir peak also indicates the existence of small Ir NPs,which is already validated by the particle size distribution analysis in HRTEM results . Furthermore, BCN broadened peak at ~23º shows the reduced crystallinity of the material, which is generally caused by the incomplete thermal polymerization/condensation that produces unreacted amino moieties. These NH_2 groups in the precursors results in surface defects in BCN during annealing, that inhibit in-plane charge mobility by causing low crystallinity.[43]

3.2 Electronic and coordination structure analysis: Surface electronic properties and element compositions of the catalyst are further analysed by X-ray photoelectron spectroscopy (XPS). The complete survey spectrum (Supplementary Information S1) confirmed the presence of Ir, B, C, and N on the surface. Furthermore, the high resolution B 1s spectra, deconvoluted into two major peaks at binding energies of 190.9 and 192 eV are attributed to $–N_2BH$ bonds and B-N bond (**Fig 2b**).[44,45] The carbon 1s spectra deconvoluted into three different species shows C-N (286.1 eV), C-B (284.9 eV) and sp^2 C=C (283.3 eV) (**Fig. 2c**). Two characteristic peaks for N 1s spectra at binding energy of 398.6 and 397.4 eV ascribed to pyridinic N and B-N respectively (**Fig. 2d**).[46-48] The high-resolution Ir 4f spectra for IrO_x-TKK and Ir-BCN is further deconvoluted into major peaks at 60.2 and 63.3 eV correspond to 4f 5/2 and 4f 7/2 respectively (**Fig. 2e**). A notable shift of 0.3 eV can be seen for Ir-BCN, which shows the existence of Ir in zero oxidation state as Ir NPs compared to IrO_x-TKK XPS spectra.[49] The electron transfer from B to Ir increases the electron density around Ir active sites, which is essential inhibiting the over oxidation of Ir under higher voltage operating conditions of PEMWEs. Thus, B restricts the over oxidation of surface Ir through surface-stabilization effects, which improves the durability of the catalyst.[50,51]

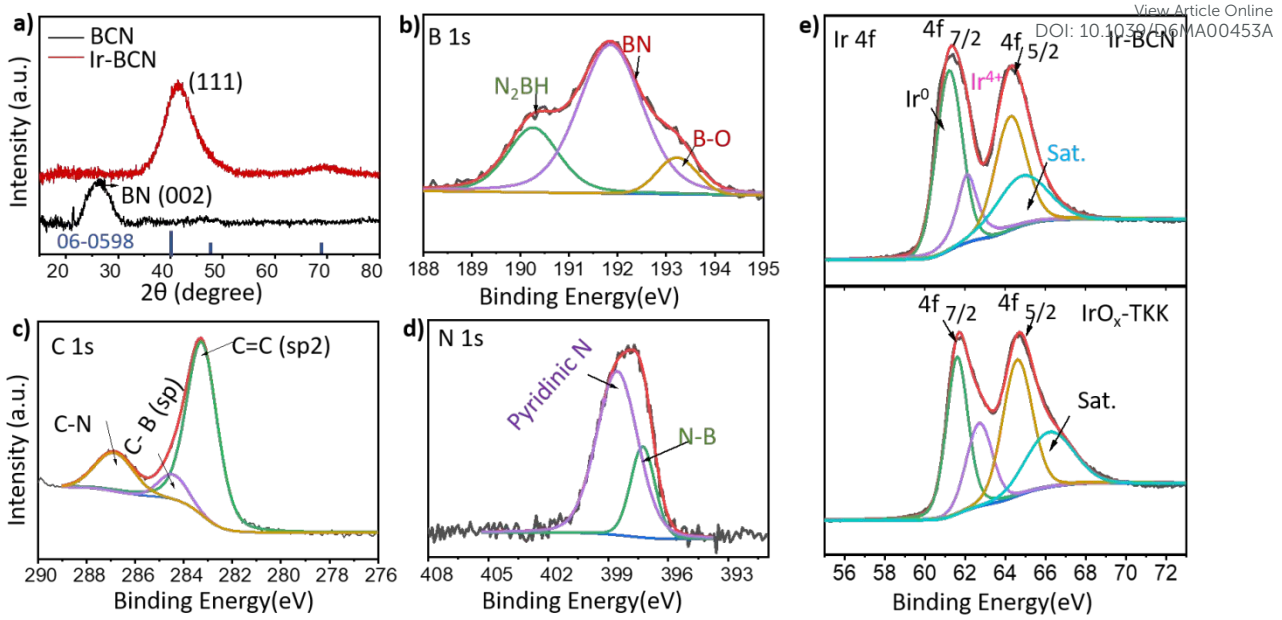

Figure 2. **Electronic structural analysis: a)** XRD pattern of BCN and Ir-BCN, XPS spectra of **b)** B1s, **c)** C1s, **d)** N1s and **e)** Ir 4f in Ir-BCN and IrO_x-TKK

3.3 Electrochemical half-cell activity and durability: Electrochemical half-cell testing carried out to assess the electrocatalytic OER properties of the Ir-BCN and benchmarked with commercial IrO_x-TKK catalyst. Cyclic voltammetry (CV) performed to calculate the ECSA (**Fig.3a**).[52] ECSA was calculated using two complementary approaches. Initially, integrated voltametric charge obtained from CV, Ir-BCN shows a higher ECSA of 108 m^2g^{-1} compared to IrO_x-TKK (83 m^2g^{-1}) due to increased active sites density of small Ir NPs uniformly dispersed over BCN support. Moreover, double layer capacitance (Cdl) calculated from CV at different scan rate (Supplementary information S2), providing a relative estimate of the electrochemically accessible surface area. The Ir-BCN catalyst exhibited a Cdl derived ECSA of 73.4 m^2g^{-1} which is higher than that of IrO_x-TKK (37.8 m^2g^{-1}). Linear sweep voltammetry measurements show the excellent OER activity of Ir-BCN with an overpotential of 240 mV at a current density of 10 mA cm^{-2} compared to IrOx (320 mV) (**Fig. 3b**). For improving the accuracy of measured electrochemical response, iR corrected potential was also shown for both catalysts (V_{iR}) which exhibit a significant difference of 10 mV overpotential. Solution resistance is calculated from the EIS Nyquist plot at high frequency region (Supplementary information S3). Superior kinetic properties are further evidenced by lower Tafel slope of 72 mV dec^{-1} (R^2= 0.987) compared to commercial IrO_x-TKK (89 mV dec^{-1}), which shows the accelerated kinetic properties of the Ir-BCN (**Fig. 3c**). Higher conductivity of BCN and metal support interaction are the key factors that facilitates electron transfer between Ir NPs and

View Article Online
DOI: 10.1039/D0MA00453A

catalyst support during the OER. A lower Tafel slope is a significant sign of an efficient electrocatalyst since it reduces the overpotential substantially for the sluggish multi-electron transfer OER reaction.[53-55] Furthermore, a detailed comparison of OER overpotential and Tafel values of Ir-BCN with recently published works shows the excellent electrocatalytic OER properties of the Ir-BCN catalyst (**Fig. 3d**) (Supplementary information Table S1).[46, 47] Similarly, the mass normalized OER activity is another important factor that determines the efficiency of the catalyst, where Ir-BCN demonstrated a mass activity of 386 A g_{Ir}^{-1} at 1.53 V which is 20 times higher than that of IrO_x-TKK catalyst (18.27 A g_{Ir}^{-1}) (**Fig. 3e**, Supplementary information S4, table S2). Higher mass activity is attributed to lower loadings with highly uniform dispersion of smaller Ir NPs on BCN support that maximizes the exposure the active sites leadings to enhanced ECSA. Furthermore, a global comparison of mass activity with recently published work shows a better mass activity Ir-BCN catalyst at the corresponding potential (**Fig. 3f**).

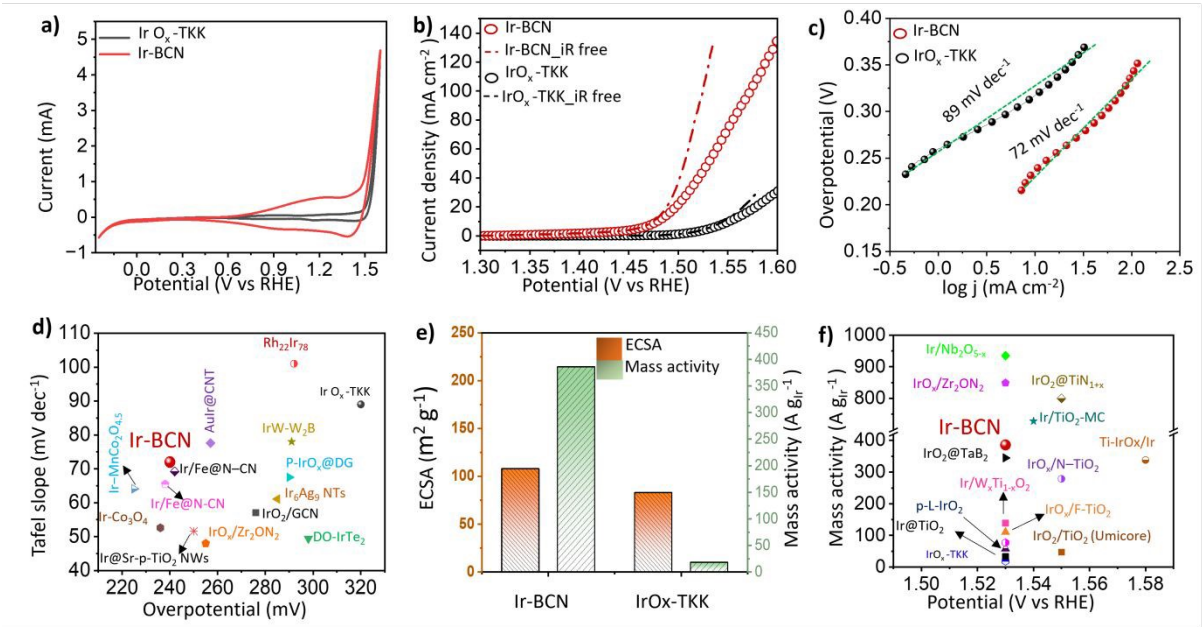

Figure 3. Electrochemical Half-cell testing in liquid electrolyte: a) CV profile for Ir-BCN and IrO_x-TKK, **b)** LSV curves of Ir-BCN and IrO_x-TKK in 0.5 M H_2SO_4 solution at scan rate of 5 mV s^{-1}, **c)** Tafel slope and **d)** corresponding comparison of overpotentials and Tafel plots of Ir-BCN and IrO_x-TKK with recently reported Ir-based OER electrocatalysts, **e)** Mass activity and ECSA comparison of Ir-BCN and IrO_x-TKK catalysts with the, **f)** Corresponding global mass activity comparison with recently published OER electrocatalyst

View Article Online
DOI: 10.1039/D0MA00453A

Electrocatalyst durability of the Ir-BCN and IrO_x-TKK is tested via chronoamperometry at 1.5 V vs RHE for 20 hours in 0.5 M H_2SO_4 where, Ir-BCN catalyst shows enhanced operational stability relative to IrO_x-TKK catalyst (**Fig. 4a**). Detailed analysis shows initial decrease in the current density is primarily associated with surface stabilization and restructuring of Ir based catalyst during the early stage of OER operation in acidic media.[51] Moreover, a slight decrease in current density occurs after 10 hours. The observed fluctuations and recovery events in the chronoamperometric profile are attributed to temporary removal of accumulated oxygen bubbles from the electrode surface, which partially restored electrolyte accessibility to active sites. The excess bubble formation and accumulation on the surface of the electrode leads to partial electrode blockage and cause a quick degradation. Corresponding retention profile (**Fig. 4b**) assessed the enhanced degradation resistance of Ir-BCN than IrO_x-TKK. Further validation of the excellent stability of Ir-BCN is evidenced by the LSV curves after 20 hours of durability testing, where Ir-BCN retains maximum current density compared to IrO_x-TKK (**Fig. 4c**).

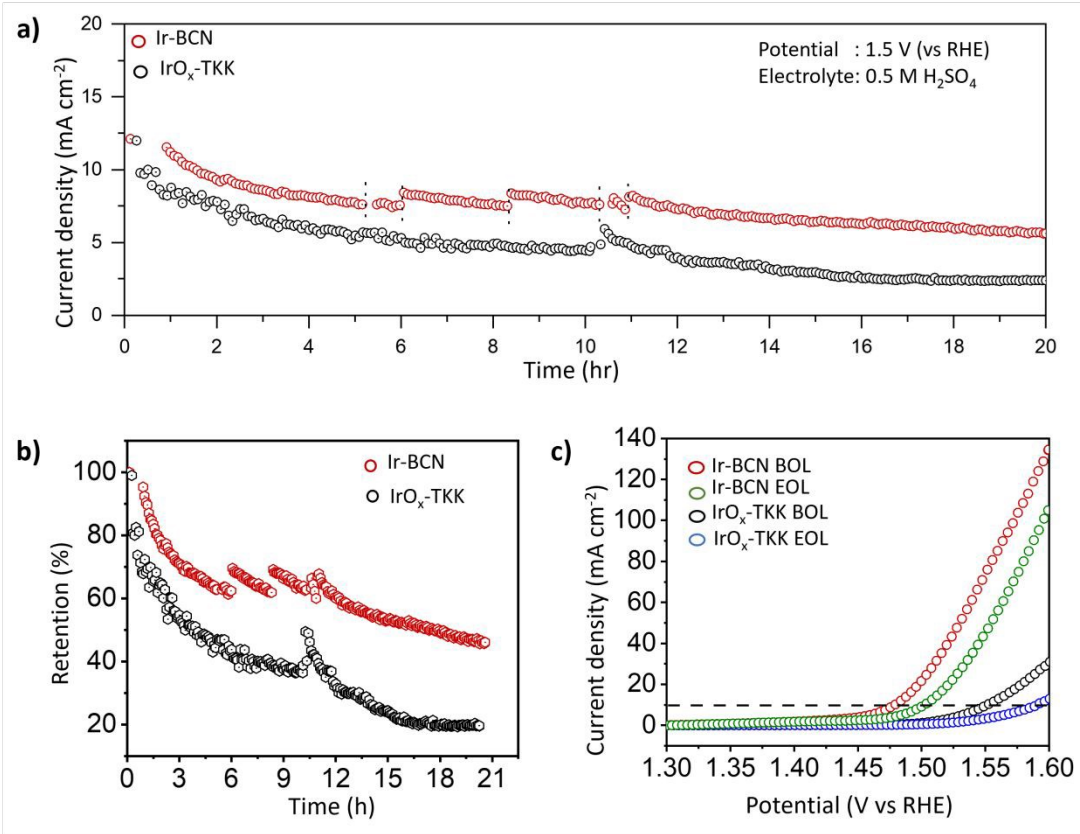

Figure 4. Half-cell Durability testing of Ir-BCN and IrO_x-TKK: a) Chronoamperometry stability evaluation of Ir-BCN and IrO_x-TKK at 1.5 V vs RHE. **b)** Corresponding retention

View Article Online
DOI: 10.1039/D6MA00453A

profile derived from chronoamperometric data, **c)** LSV curve of Ir-BCN and IrO_x-TKK before and after stability test.

The corrosion resistance characteristics of Ir-BCN and IrO_x-TKK have been further assessed under realistic operating conditions using the potentiodynamic polarisation method.[56] A three electrode cell was setup to measure the corrosion behaviour of the electrocatalyst with Hg/Hg_2SO_4 as reference electrode (with a potential of 0.650 V) and graphite electrode as Counter electrode in a 0.5 M H_2SO_4 at 80 °C **(fig. 5a)**. (All the values in electrochemical studies are tabulated in the supplementary information Table S3). In this setup, the corrosion resistance of the materials is evaluated over a range of potential, where the corrosion current is used an assessment for the anti-corrosion behaviour of material (**fig. 5b**). Ir-BCN revealed superior corrosion resistance than of IrO_x-TKK, with corrosion current density (i_{corr}) of 182.88 µA cm^{-2} compared to IrO_x-TKK i_{corr} (329.83 µA cm^{-2}), demonstrating the improved corrosion resistance of BCN support material.

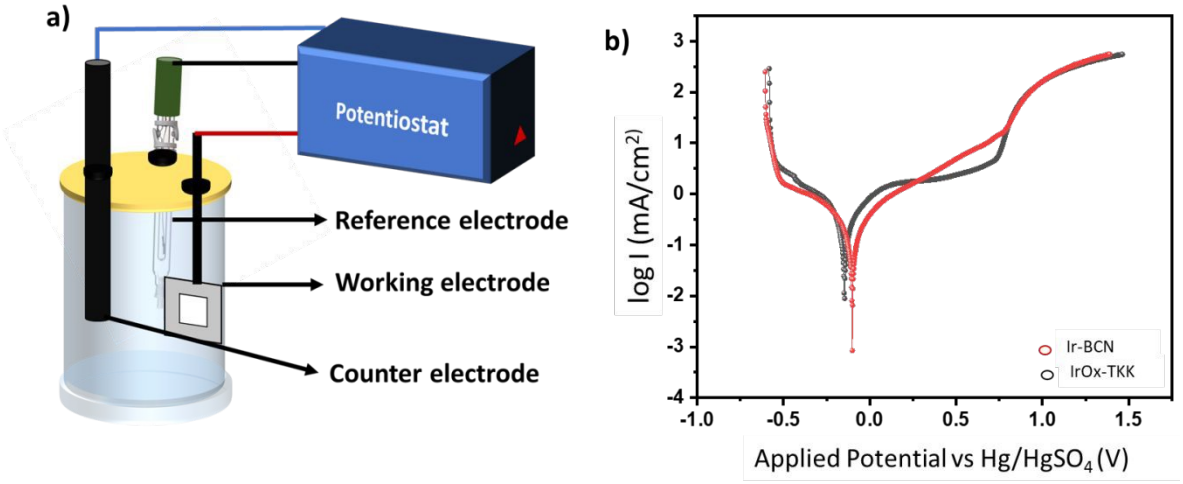

Figure 5. Corrosion testing result of Ir-BCN and IrO_x-TKK. **a)** Three electrode cell for evaluating corrosion characteristic, **b)** Potentiodynamic polarization curve of IrO_x-TKK and Ir-BCN in 0.5 M H_2SO_4 at 80 ^{O}C.

3.4 Ir-BCN single cell test: To further investigate the potential of Ir-BCN as anodic catalyst, we have assembled the Ir-BCN as anode CL in a membrane electro assembly (MEA) . Ir-BCN was used as anode CL and Pt/C TKK as cathode CL, are spray coated on Nafion membrane (N-115) on a 5 cm^2 active area. The MEA consist of catalyst coated membrane sandwiched between the anode porous transport layer (Pt-coated titanium felt) and carbon microporous

View Article Online
DOI: 10.1039/D6MA00453A

layer (Carbon paper MPL) at cathode CL (Supplementary information S5 a). For comparison, another MEA with IrO_x-TKK as anode CL and Pt/C TKK as cathode CL were assembled and tested under similar conditions. The cell was conditioned for 5 hours with constant current and voltage hold protocols before measuring the beginning of life polarization curves to ensure the catalyst activation and stabilization of the cell. Polarization curves for Ir-BCN and IrO_x-TKK were recorded via galvanostatic polarization in a current density range of 0.1 to 3 A cm^{-2} at 80 °C. Electrochemical impedance spectroscopy (EIS) was performed to assess the cell voltage losses at different current density in frequency range of 100 kHz to 100 mHz. Ohmic losses due to membrane and cell components are corrected by high frequency resistance (HFR) for both samples. The polarization curves show superior cell performance for Ir-BCN compared to IrO_x-TKK with lower cell voltage at the respective current density (**Fig. 6a)**. The cell voltage for Ir-BCN as anode CL at current density 2.0 A cm^{-2} is 1.85 V, which is significantly lower than IrO_x-TKK that has exhibited the cell voltage of 2.12 V at 2.0 A cm^{-2}, demonstrating the superior performance under similar Ir loadings.

Furthermore, the cell resistance measured via EIS are used for the detailed analysis of voltage losses (ohmic, kinetic and mass transport losses) within the PEMWEs system. HFR in typical EIS data represents the voltage losses due to ohmic resistance contributed mainly by the charge transfer resistance, the resistance to proton transfer across the membrane and interfacial resistance within the MEA. Both MEAs, Ir-BCN and IrO_x-TKK show similar HFR values with the Ir-BCN MEA slightly higher HFR than of IrO_x-TKK (0.166 vs 0.162 Ω cm^2), yet, these differences are insignificant (Supplementary information S5 b). HFR free voltage is calculated using $V_{Ohmic\ free}=V-\eta ohmic,\ \eta ohmic=i\times HFR$, which shows a significant impact of the ohmic resistance on the cell voltage. The HFR-free polarization curves shows that Ir-BCN MEA has significantly lower cell voltage compared to IrO_x-TKK MEA at the corresponding current density. Ir-BCN MEA achieved a voltage of 1.52 V at the current density of 2.0 A cm^{-2}, which is substantially lower than that of IrO_x-TKK that shows a minimum voltage of 1.81 V for 2.0 A cm^{-2} current density. After ohmic loss determination, we have further performed the cell voltage breakdown into kinetic and mass transport losses to find out the individual contributions by the kinetic and mass transport resistances. The calculations are performed according to our previous work.[57] Cell voltage breakdown plots show the detailed comparison of voltage losses contributed by kinetic, ohmic and mass transport for both samples (**Fig. 6b**). The kinetic loss for Ir-BCN based MEA is significantly lower than IrO_x-TKK, which shows the superior kinetic properties of the Ir-BCN catalyst. Kinetic losses increase for both MEAs in the low current density region and become stable at higher current density with insignificant

View Article Online
DOI: 10.1039/D6MA00453A

changes beyond 100 mAcm^{-2} due to dominant effect of ohmic and mass transport losses.58 Superior kinetic properties of the Ir-BCN are also evidenced by the lower Tafel slope (38 mV dec^{-1}) as compared to IrO_x-TKK (76 mV dec^{-1}) (Supplementary information S5 (c,d)) which indicates conductive BCN support improves the charge transfer properties between BCN and Ir NPs.[21] Ohmic loss for both the samples are same as expected which are mainly contributed by the membrane and other interfacial resistances which observed to be similar for both MEAs under similar testing conditions.

Finally, the mass transport loss for Ir-BCN is found to be lower than IrO_x-TKK, indicating the better mass transport features of Ir-BCN based CL. For Ir-BCN CL the mass transport loss is lower, and it kept increasing with increase in current density. However, even at high current density the mass transport loss for Ir-BCN is significantly lower than IrO_x-TKK based CL demonstrating superior mass transport properties of the Ir-BCN CL. This could be ascribed to uniform dispersion of Ir NPs on porous architecture of the BCN support that facilitates the active sites accessibility under dynamic conditions of higher current density. Ohmic losses predominant contributor at high current densities, suggesting that the membrane and contact resistance significantly limit overall efficiency under high load conditions (Supplementary information S6). The percentage contributions of individual losses shows that the small but non-negotiable undefined losses indicate the presence of additional factors such as mass transport limitation or interfacial phenomena, which needs further investigation. Figure 6c describes the percentage comparison for the different losses for Ir-BCN and IrO_x-TKK.

Both the catalysts were also run for long term stability test via steady-state operational stability test at a constant current of 1 A cm^{-2} by chronopotentiometry (CP) measurements at 80 °C. Ir-BCN CL shows superior durability to that of the IrO_x-TKK based MEA over the course of 575 hours with degradation rate of 104.3 µV hour^{-1} compared to IrO_x-TKK that degrades significantly after the 542 hours with a degradation rate of 405.9 µV hour^{-1} (**Fig. 6d**). For a direct comparison over the same operating duration, degradation rate for Ir-BCN is also calculated at 542 hours, which is 102.7 µV hour^{-1}. Results were compared with recently published works (Supplementary information, Table S6). Polarisation curves for Ir-BCN at the beginning and after 575 hours of stability test implicate excellent catalyst durability (**Fig. 6e**). An increase in cell voltage in the high current density region is observed, which is attributed to changes in CL structures leading to poor mass transfer properties. Interestingly, the low current density region shows the similar performance after durability test demonstrating the stable kinetic properties of Ir-BCN. To further assess the voltage losses that contribute to overall cell voltage loss, we have performed the cell voltage breakdown after durability testing. As

observed in polarization curves, there is negligible changes in the kinetic and ohmic losses before and after the durability for Ir-BCN (Supplementary information S8). However, a significantly higher mass transport loss is observed after durability studies, which indicates that the Ir-BCN architecture might be disrupted that resulted in mass transport loss at higher current density regime.

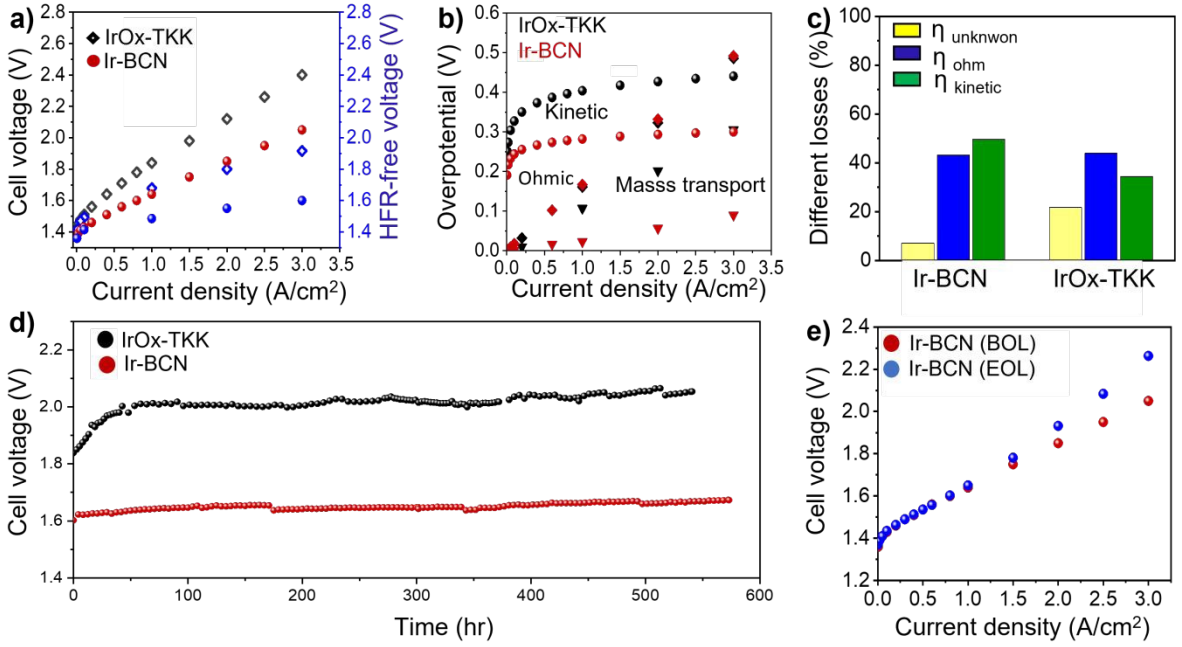

Figure 6. **PEMWEs performance in full cell test: a)** Polarisation curve for Ir-BCN and IrO_x-TKK at 80 °C with Nafion 115, **b)** Contributions of ohmic, kinetic and mass transport overpotentials as a function of current density, **c)** corresponding values of ohmic, kinetic and mass transport loses, **d)** Chronopotentiometry curves of Ir-BCN and IrO_x-TKK catalyst layers in MEA operated at 1 A cm^{-2} at 80 °C. **e)** Beginning of life and end of life polarisation curve for Ir-BCN.

A post durability morphology evaluation was carried out via HR-TEM and EDS mapping measurements by collecting the Ir-BCN catalyst from anode CL after 575 hours of durability test. TEM shows the spherical morphology of the Ir NPs, which implies similar morphology studied before the beginning of life performance of Ir-BCN catalyst (**Fig 7a, b, c).** There is no obvious aggregation of the NPs which further evidenced the strong anchoring of Ir NPs to the BCN support. Particle size distribution shows the average size of 2-5 nm, which is slightly larger than BOL morphology analysis, yet the changes are insignificant and indicates the excellent stability of the Ir-BCN catalyst (**Fig. 7d**). Furthermore, the EDS mapping of the

View Article Online
DOI: 10.1039/D6MA00453A

elemental distribution in Ir-BCN also shows uniform distribution of elements specifically the Ir in Ir-BCN catalyst indicating the insignificant changes in the overall catalyst nanostructure (**Fig. 7e**).

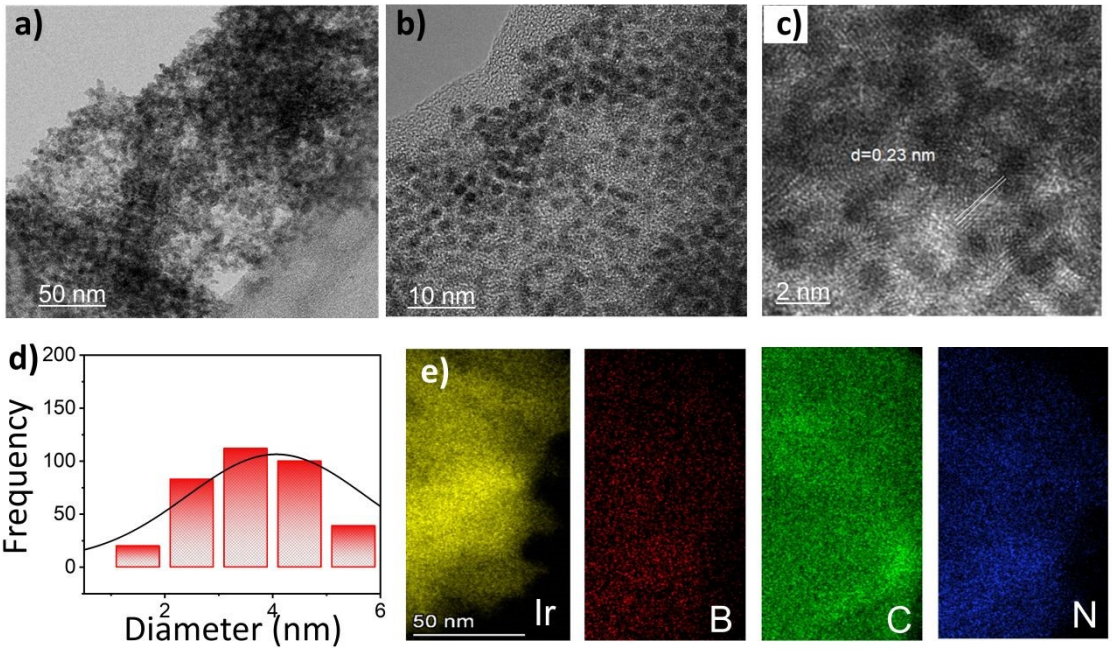

Figure 7. Post durability morphology analysis of Ir-BCN: a-c) TEM and HR-TEM analysis, **d)** Particle size distribution, **e)** EDS elemental mapping after the durability testing at 1 A cm^{-2} at 80 °C.

4. Conclusion

In summary, the Ir-BCN catalyst demonstrates that reducing Ir loading without compromising stability is achievable through strong metal–support interactions and the conductive nanoarchitecture of BCN. Uniformly dispersed Ir nanoparticles (2–3 nm) on BCN deliver enhanced OER kinetics and improved durability compared to commercial IrOx–TKK. Particularly, under standard PEMWEs operating conditions, the Ir-BCN based anode catalyst layer achieves higher current density at lower cell voltage with minimal kinetic and mass transport losses and excellent electrochemical stability over long-term operation. Voltage breakdown analysis confirmed no significant changes in the overall ohmic, kinetic and mass transport losses over the course of long-term durability. Similarly, corrosion testing confirmed the superior anti-corrosion capability of the Ir-BCN catalyst, further supported by post-durability morphology analysis showing excellent structural integrity of the Ir-BCN catalyst layer after prolonged operation. These findings highlight Ir-BCN as a promising low-Ir, durable anode catalyst for efficient PEMWEs.

View Article Online
DOI: 10.1039/D6MA00453A

Conflicts of interest

The Authors declare no competing interests.

Acknowledgements:

We would like to acknowledge the support of the Natural Sciences and Engineering Research Council of Canada (NSERC), Canada Research Chair (CRC-2019-00354), Discovery grant (CRSNG-DGECR-2022-00058) and Mitacs Accelerate (IT25281).

View Article Online
DOI: 10.1039/D6MA00453A

References

1. Wang, L., Pan, Q., Liang, X., and Zou, X. (2024). Ensuring stability of anode catalysts in PEMWE: from material design to practical application. ChemSusChem, e202401220.
2. Kumar, S.S., and Lim, H. (2023). Recent advances in hydrogen production through proton exchange membrane water electrolysis–a review. Sustainable Energy & Fuels *7*, 3560-3583.
3. Wang, C.R., Stansberry, J.M., Mukundan, R., Chang, H.-M.J., Kulkarni, D., Park, A.M., Plymill, A.B., Firas, N.M., Liu, C.P., and Lang, J.T. (2025). Proton exchange membrane (PEM) water electrolysis: cell-level considerations for gigawatt-scale deployment. Chemical Reviews *125*, 1257-1302.
4. Maniscalco, M.P., Longo, S., Cellura, M., Miccichè, G., and Ferraro, M. (2024). Critical review of life cycle assessment of hydrogen production pathways. Environments *11*, 108.
5. Varsha, K., and Kiran, G. (2025). A ligand-specific bimetallic electrocatalyst for efficient oxygen evolution reaction at higher current density. Sustainable Energy & Fuels *9*, 2287-2293.
6. Aralekallu, S., Lokesh, K.S., and Singh, V. (2024). Advanced bifunctional catalysts for energy production by electrolysis of earth-abundant water. Fuel *357*, 129753.
7. Yang, C., Pang, H., Li, X., Zheng, X., Wei, T., Ma, X., Wang, Q., Wang, C., Wang, D., and Xu, B. (2025). Scalable electrocatalytic urea wastewater treatment coupled with hydrogen production by regulating adsorption behavior of urea molecule. Nano-Micro Letters *17*, 159.
8. Lala, S.R.F., and Shahgaldi, S. (2025). Mass and charge transport phenomena in porous transport layer for proton exchange membrane water electrolyzers: A review. Energy Reports *13*, 162-183.
9. Huang, R., Wen, Y., Miao, P., Shi, W., Niu, W., Sun, K., Li, Y., Ji, Y., and Zhang, B. (2023). Constructing the oxygen diffusion paths for promoting the stability of acidic water oxidation catalysts. Chem Catalysis *3*.
10. Lim, A., Ham, K., Quast, T., Lee, S., Tesch, M.F., Czioska, S., Ramermann, D., Hetaba, W., Schuhmann, W., and Grunwaldt, J.-D. (2025). Limited Surface Oxide Growth as a

Prerequisite for Stabilizing Low-Loading Iridium Electrodes for PEM Water Electrolysis. ACS Catalysis *15*, 6098-6113.

11. Chen, C., Wang, X., Huang, Z., Mo, J., Zhang, X., Peng, C., Khairy, M., Ge, J., and Long, Z. (2024). Engineering of self-supported electrocatalysts on a three-dimensional nickel foam platform for efficient water electrolysis. Transactions of Tianjin University *30*, 103-116.
12. Bernt, M., Hartig-Weiß, A., Tovini, M.F., El-Sayed, H.A., Schramm, C., Schröter, J., Gebauer, C., and Gasteiger, H.A. (2020). Current challenges in catalyst development for PEM water electrolyzers. Chemie Ingenieur Technik *92*, 31-39.
13. Hansen, K.U., Lee, A., and Jiao, F. (2024). Enabling low-IrO2 proton exchange membrane water electrolysis via microporous layer-supported catalyst-coated membranes. Chem Catalysis *4*.
14. Cherevko, S. (2023). Stabilization of non-noble metal electrocatalysts for acidic oxygen evolution reaction. Current Opinion in Electrochemistry *38*, 101213.
15. Liu, T., Chen, C., Pu, Z., Huang, Q., Zhang, X., Al-Enizi, A.M., Nafady, A., Huang, S., Chen, D., and Mu, S. (2024). Non-Noble-Metal-Based Electrocatalysts for Acidic Oxygen Evolution Reaction: Recent Progress, Challenges, and Perspectives. Small *20*, 2405399.
16. Zaman, S., Moradizadeh, L., Murugaiah, D.K., Khalid, M., Roohan Farooq Lala, S., and Shahgaldi, S. (2026). Exploring the degradation of catalyst layer and porous transport layer in proton exchange membrane water electrolyzers. EES Catalysis *4*, 11-30. 10.1039/d5ey00270b.
17. Ko, W., Shim, J., Ahn, H., Kwon, H.J., Lee, K., Jung, Y., Antink, W.H., Lee, C.W., Heo, S., and Lee, S. (2025). Controlled Structural Activation of Iridium Single Atom Catalyst for High-Performance Proton Exchange Membrane Water Electrolysis. Journal of the American Chemical Society.
18. Wang, D., Lin, F., Luo, H., Zhou, J., Zhang, W., Li, L., Wei, Y., Zhang, Q., Gu, L., and Wang, Y. (2025). Ir-O-Mn embedded in porous nanosheets enhances charge transfer in low-iridium PEM electrolyzers. Nature Communications *16*, 181.
19. Choi, J.Y., Kim, J.G., Lee, H.J., and Pak, C. (2025). Advanced iridium catalysts on multi-porous tantalum oxide supports for efficient proton exchange membrane water electrolysis. International Journal of Hydrogen Energy *97*, 57-65.

20. Belami, D., Lindley, M., Jonnalagadda, U.S., Goncalves Bullock, A.M., Fan, Q., Liu, W., Haigh, S.J., Kwan, J., Regmi, Y.N., and King, L.A. (2024). Active and highly durable supported catalysts for proton exchange membrane electrolysers. EES Catal. *2*, 1139-1151. 10.1039/d4ey00026a.

21. Shi, Z., Li, J., Jiang, J., Wang, Y., Wang, X., Li, Y., Yang, L., Chu, Y., Bai, J., Yang, J., et al. (2022). Enhanced acidic water oxidation by dynamic migration of oxygen species at the Ir/Nb_2O_{5-x} catalyst/support interfaces. Angew. Chem. Int. Ed. *61*, e202212341. 10.1002/anie.202212341.

22. Zaman, S., Khalid, M., and Shahgaldi, S. (2024). Advanced electrocatalyst supports for proton exchange membrane water electrolyzers. ACS Energy Lett., 2922-2935. 10.1021/acsenergylett.4c00275.

23. Yang, L., Wang, R., and Tang, C. (2023). Innovating support and interface for low-iridium catalysts in practical PEM electrolyzers. Chem Catalysis *3*.

24. Zaman, S., Wang, M., Liu, H., Sun, F., Yu, Y., Shui, J., Chen, M., and Wang, H. (2022). Carbon-based catalyst supports for oxygen reduction in proton-exchange membrane fuel cells. Trends in Chemistry *4*, 886-906.

25. Zaman, S., Su, Y.Q., Dong, C.L., Qi, R., Huang, L., Qin, Y., Huang, Y.C., Li, F.M., You, B., and Guo, W. (2022). Scalable molten salt synthesis of platinum alloys planted in metal–nitrogen–graphene for efficient oxygen reduction. Angewandte Chemie International Edition *61*, e202115835.

26. Jorge, A.B., Dedigama, I., Miller, T.S., Shearing, P., Brett, D.J., and McMillan, P.F. (2018). Carbon nitride materials as efficient catalyst supports for proton exchange membrane water electrolyzers. Nanomaterials *8*, 432.

27. Chen, J., Cui, P., Zhao, G., Rui, K., Lao, M., Chen, Y., Zheng, X., Jiang, Y., Pan, H., and Dou, S.X. (2019). Low-coordinate iridium oxide confined on graphitic carbon nitride for highly efficient oxygen evolution. Angewandte Chemie International Edition *58*, 12540-12544.

28. Wu, Y., Yao, R., Zhao, Q., Li, J., and Liu, G. (2023). RuO 2 nanoparticles anchored on gC 3 N 4 as an efficient bifunctional electrocatalyst for water splitting in acidic media. Dalton Transactions *52*, 10515-10521.

29. Jiang, B., Wang, T., Cheng, Y., Liao, F., Wu, K., and Shao, M. (2018). Ir/g-C3N4/nitrogen-doped graphene nanocomposites as bifunctional electrocatalysts for overall water splitting in acidic electrolytes. ACS applied materials & interfaces *10*, 39161-39167.

30. Wang, S., Lv, H., Tang, F., Sun, Y., Ji, W., Zhou, W., Shen, X., and Zhang, C. (2021). Defect engineering assisted support effect: IrO2/N defective g-C3N4 composite as highly efficient anode catalyst in PEM water electrolysis. Chemical Engineering Journal *419*, 129455.

31. Wu, J., Liu, Z., Lin, X., Jiang, E., Zhang, S., Huo, P., Yan, Y., Zhou, P., and Yan, Y. (2022). Breaking through water-splitting bottlenecks over carbon nitride with fluorination. Nat Commun *13*, 6999. 10.1038/s41467-022-34848-8.

32. Nehate, S., Saikumar, A., Prakash, A., and Sundaram, K. (2020). A review of boron carbon nitride thin films and progress in nanomaterials. Materials Today Advances *8*, 100106.

33. Wang, S., Wang, G., Wu, T., Zhang, Y., Zhan, F., Wang, Y., Wang, J., Fu, Y., and Qiu, J. (2018). BCN nanosheets templated by gC 3 N 4 for high performance capacitive deionization. Journal of Materials Chemistry A *6*, 14644-14650.

34. Zhao, D., Wang, Y., Dong, C.-L., Huang, Y.-C., Chen, J., Xue, F., Shen, S., and Guo, L. (2021). Boron-doped nitrogen-deficient carbon nitride-based Z-scheme heterostructures for photocatalytic overall water splitting. Nature Energy *6*, 388-397. 10.1038/s41560-021-00795-9.

35. Zhao, X., Mou, T., Long, J., Islam, A., Kang, S., Kariuki, N.N., Myers, D.J., Liu, P., Rodriguez, J.A., Chen, J.G., and Sasaki, K. (2025). Strong Coupling of Iridium and Boron-Carbon-Nitride Support for Enhanced Acidic Water Oxidation. J Am Chem Soc *147*, 43317-43329. 10.1021/jacs.5c08243.

36. Torres-Pinto, A., Díez, A.M., Silva, C.G., Faria, J.L., Sanromán, M.Á., Silva, A.M.T., and Pazos, M. (2024). Tuning graphitic carbon nitride (g-C3N4) electrocatalysts for efficient oxygen evolution reaction (OER). Fuel *360*. 10.1016/j.fuel.2023.130575.

37. Yue, L., Guo, H., Hua, J., Yu, M., Liu, K., Yang, X., Liu, J., and Cheng, J. (2024). An N-defective graphitic carbon nitride-supported Ir/Fe catalyst with low Ir-content as highly efficient oxygen evolution reaction catalyst for acidic water splitting. Electrochimica Acta *476*. 10.1016/j.electacta.2023.143677.

38. Peng, D., Jiang, W., Li, F.-F., Zhang, L., Liang, R.-P., and Qiu, J.-D. (2018). One-pot synthesis of boron carbon nitride nanosheets for facile and efficient heavy metal ions removal. ACS Sustainable Chemistry & Engineering *6*, 11685-11694.

39. Karimi, F., and Peppley, B.A. (2017). Comparison of conventional versus microwave heating for polyol synthesis of supported iridium based electrocatalyst for polymer

electrolyte membrane water electrolysis. International Journal of Hydrogen Energy *42*, 5083-5094.

40. Dong, H., Chen, Y.-C., and Feldmann, C. (2015). Polyol synthesis of nanoparticles: status and options regarding metals, oxides, chalcogenides, and non-metal elements. Green chemistry *17*, 4107-4132.
41. Zhang, T., Li, S.-C., Zhu, W., Ke, J., Yu, J.-W., Zhang, Z.-P., Dai, L.-X., Gu, J., and Zhang, Y.-W. (2016). Iridium ultrasmall nanoparticles, worm-like chain nanowires, and porous nanodendrites: One-pot solvothermal synthesis and catalytic CO oxidation activity. Surface Science *648*, 319-327.
42. Wang, Q., Xu, C.-Q., Liu, W., Hung, S.-F., Bin Yang, H., Gao, J., Cai, W., Chen, H.M., Li, J., and Liu, B. (2020). Coordination engineering of iridium nanocluster bifunctional electrocatalyst for highly efficient and pH-universal overall water splitting. Nature Communications *11*, 4246.
43. Li, Y., Gu, M., Zhang, X., Fan, J., Lv, K., Carabineiro, S.A., and Dong, F. (2020). 2D g-C3N4 for advancement of photo-generated carrier dynamics: status and challenges. Materials Today *41*, 270-303.
44. Chang, B., Li, L., Shi, D., Jiang, H., Ai, Z., Wang, S., Shao, Y., Shen, J., Wu, Y., and Li, Y. (2021). Metal-free boron carbonitride with tunable boron Lewis acid sites for enhanced nitrogen electroreduction to ammonia. Applied Catalysis B: Environmental *283*, 119622.
45. Wang, W., Zhou, H., Liu, Y., Zhang, S., Zhang, Y., Wang, G., Zhang, H., and Zhao, H. (2020). Formation of B□ N□ C Coordination to Stabilize the Exposed Active Nitrogen Atoms in g-C3N4 for Dramatically Enhanced Photocatalytic Ammonia Synthesis Performance. Small *16*, 1906880.
46. Luo, Z., Fang, Y., Zhou, M., and Wang, X. (2019). A borocarbonitride ceramic aerogel for photoredox catalysis. Angewandte Chemie International Edition *58*, 6033-6037.
47. Song, L., Liu, Z., Reddy, A.L.M., Narayanan, N.T., Taha-Tijerina, J., Peng, J., Gao, G., Lou, J., Vajtai, R., and Ajayan, P.M. (2012). Binary and ternary atomic layers built from carbon, boron, and nitrogen. Advanced Materials *24*, 4878-4895.
48. Rao, C.N.R., and Chhetri, M. (2019). Borocarbonitrides as metal-free catalysts for the hydrogen evolution reaction. Advanced materials *31*, 1803668.
49. Fang, D., Zhang, H., He, L., Geng, J., Song, W., Sun, S., Shao, Z., and Yi, B. (2019). Facile synthesis of nanoporous Pt-encapsulated Ir black as a bifunctional oxygen

View Article Online
DOI: 10.1039/D6MA00453A

catalyst via modified polyol process at room temperature. ChemElectroChem *6*, 3633-3643.

50. Cheng, J., Yang, J., Kitano, S., Juhasz, G., Higashi, M., Sadakiyo, M., Kato, K., Yoshioka, S., Sugiyama, T., Yamauchi, M., and Nakashima, N. (2019). Impact of Ir-Valence Control and Surface Nanostructure on Oxygen Evolution Reaction over a Highly Efficient Ir–TiO2 Nanorod Catalyst. ACS Catalysis *9*, 6974-6986. 10.1021/acscatal.9b01438.
51. Chen, F.-Y., Wu, Z.-Y., Adler, Z., and Wang, H. (2021). Stability challenges of electrocatalytic oxygen evolution reaction: From mechanistic understanding to reactor design. Joule *5*, 1704-1731. 10.1016/j.joule.2021.05.005.
52. Dhawan, H., Tan, X., Shen, J., Woodford, J., Secanell, M., and Semagina, N. (2024). Strong Metal-Support Interactions in ZrO2-Supported IrOx Catalyst for Efficient Oxygen Evolution Reaction. ChemCatChem *16*, e202300668.
53. Shinagawa, T., Garcia-Esparza, A.T., and Takanabe, K. (2015). Insight on Tafel slopes from a microkinetic analysis of aqueous electrocatalysis for energy conversion. Scientific reports *5*, 13801.
54. Lei, Z., Wang, T., Zhao, B., Cai, W., Liu, Y., Jiao, S., Li, Q., Cao, R., and Liu, M. (2020). Recent progress in electrocatalysts for acidic water oxidation. Advanced energy materials *10*, 2000478.
55. Bai, X., Zhang, X., Sun, Y., Huang, M., Fan, J., Xu, S., and Li, H. (2023). Low ruthenium content confined on boron carbon nitride as an efficient and stable electrocatalyst for acidic oxygen evolution reaction. Angewandte Chemie International Edition *62*, e202308704.
56. Vílchez-Cózar, Á., Colodrero, R.M.P., Bazaga-García, M., Marrero-López, D., El-refaei, S.M., Russo, P.A., Pinna, N., Olivera-Pastor, P., and Cabeza, A. (2023). Tuning the activity of cobalt 2-hydroxyphosphonoacetates-derived electrocatalysts for water splitting and oxygen reduction: Insights into the local order by pair distribution function analysis. Applied Catalysis B: Environmental *337*. 10.1016/j.apcatb.2023.122963.
57. Gupta, A., Chellehbari, Y.M., and Shahgaldi, S. (2025). Achieving high performance and durability with ultra-low precious metal nanolayer on porous transport layer for PEMWE application. J. Power Sources *630*, 236088. 10.1016/j.jpowsour.2024.236088.
58. Suermann, M., Schmidt, T.J., and Büchi, F.N. (2016). Cell Performance Determining Parameters in High Pressure Water Electrolysis. Electrochimica Acta *211*, 989-997. 10.1016/j.electacta.2016.06.120.

View Article Online
DOI: 10.1039/D6MA00453A

View Article Online
DOI: 10.1039/D6MA00453A

The supporting data has been provided as part of the Supplementary information